Showcasing research from Professor Se-Hun Kwon's laboratory, School of Materials Science and Engineering, Pusan National University, Republic of Korea.

Controllable size and crystallinity of Ru nanoparticles on a carbon support synthesized by fluidized bed reactor-atomic layer deposition for enhanced hydrogen oxidation activity

Carbon-supported controllable size and crystallinity Ru nanoparticles were synthesized by fluidized bed reactor atomic layer deposition (FBR-ALD) for the application of the anion exchange membrane fuel cells. FBR-ALD synthesized Ru nanoparticles with a uniform size of about 2.2 nm exhibited an enhanced hydrogen oxidation reaction, mass and specific activity under alkaline condition due to its highly electrochemically active roughened surfaces.

As featured in:

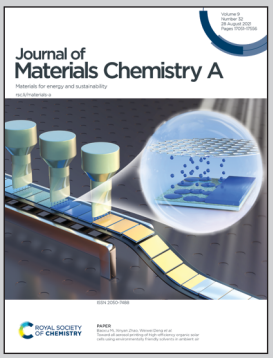

See Se-Hun Kwon *et al.*, *J. Mater. Chem. A*, 2021, **9**, 17223.

ROYAL SOCIETY OF CHEMISTRY

rsc.li/materials-a

Registered charity number: 207890

Journal of Materials Chemistry A

ROYAL SOCIETY OF CHEMISTRY

PAPER

View Article Online
View Journal | View Issue

Open Access Article. Published on 21 June 2021. Downloaded on 2/16/2026 10:57:02 AM.
This article is licensed under a Creative Commons Attribution-NonCommercial 3.0 Unported Licence.

Check for updates

Cite this: J. Mater. Chem. A, 2021, 9, 17223

Controllable size and crystallinity of Ru nanoparticles on a carbon support synthesized by fluidized bed reactor-atomic layer deposition for enhanced hydrogen oxidation activity†

Woo-Jae Lee,[ab] Susanta Bera,[ab] Hyun-Jae Woo,[b] Jung-Won An,[b] Jong-Seong Bae,[c] Il-Kwon Oh[d] and Se-Hun Kwon *[ab]

Received 1st May 2021
Accepted 19th June 2021

DOI: 10.1039/d1ta03678e

rsc.li/materials-a

Low-temperature fuel cells have attracted significant attention owing to their low cost and high performance. Herein, uniform Ru nanoparticles (NPs) with various size distributions were synthesized as a non-Pt catalyst on a carbon support by fluidized bed reactor-atomic layer deposition (FBR-ALD) as a function of ALD cycles for the hydrogen oxidation reaction (HOR) in alkaline medium. With an increase in the number of ALD cycles from 5 to 30 cycles, the wt% of the Ru NPs increased from ~5 to ~32 wt%. In addition, the structural characterization of the Ru NPs revealed the formation of Ru NPs with a uniform, dense, and controllable size (~2–4 nm) and crystallinity depending on the growth cycle of ALD. However, the 10 cycled Ru catalyst with a NP size of ~2 nm possessed a highly electrochemically active roughened surface (amorphous moiety covered the crystallite), which enhanced its HOR and mass activity. Remarkably, the ALD-synthesized Ru catalyst outperformed a commercial Ru/C catalyst with a similar wt%. Hydrogen binding energy (HBE) calculations revealed that the specific activity of the catalyst increased with decreasing HBE. The mechanistic pathway for the HOR indeed illustrates that enhanced activity under alkaline conditions was found owing to the weakening of the metal–H interaction influenced by the Ru NP crystallinity and size. The findings of this study indicate that the FBR-ALD technique is an effective, scalable approach for the synthesis of active non-Pt metal catalysts.

1. Introduction

Low-temperature fuel cell technology has attracted tremendous attention owing to its promising energy sources for a wide range of applications, particularly in portable electronic devices and automobiles.[1] There are two types of membrane fuel cells based on the types of ion exchange membranes employed in the cells: proton exchange membrane fuel cells (PEMFCs) and anion exchange membrane fuel cells (AEMFCs).[2] In contrast to PEMFCs, which uses an acidic membrane, AEMFCs are regarded as low-cost fuel cells that use an alkaline membrane[3,4] because Pt-free catalysts are used to perform the oxygen reduction reaction (ORR) and hydrogen oxidation reaction (HOR) in AEMFCs owing to their lower activation energy in alkaline media. However, compared with the extensive research studies available on PEMFCs, studies on AEMFCs are still challenging and adventurous,[5] and there are several factors that limit the commercialization of AEMFCs.[6] Especially, there are no appropriate and efficient anode catalysts that can control the sluggish HOR reaction at the anode of AEMFCs compared to the ORR at the cathode.[7]

Some studies have demonstrated that the activity of Pt catalysts in AEMFCs decreases by ~2 orders of magnitude when they move from an acidic (pH = 0) to a basic (pH = 13) medium.[8] Nevertheless, over 95% of the studies on AEMFCs have focused on the use of Pt and Pt-based catalysts, and only a few studies have reported on the use of Pt-free catalysts.[5] Among several Pt-free catalysts that can be used in AEMFCs, Ru nanoparticles (NPs) have been considered as one of the most promising candidates.[9] Generally, Ru NPs are synthesized on carbon supports by a wet-based method.[10–12] In addition, they exhibit improved performance compared to Pt catalysts in alkaline media owing to their stronger binding energy to metal–H bonds under abundant OH– conditions.[10] However, the synthesis of Ru NPs by the wet-chemical process reduces the uniformity of Ru NPs, and significantly affects their catalytic activity. The size and crystallinity of NPs have been identified as

[a]Institute of Materials Technology, Pusan National University, 30 Jangjeon-Dong Geumjeong-Gu, Busan 46241, Republic of Korea. E-mail: sehun@pusan.ac.kr
[b]School of Materials Science and Engineering, Pusan National University, 30 Jangjeon-Dong Geumjeong-Gu, Busan 46241, Republic of Korea
[c]Busan Center, Korea Basic Science Institute, Busan 46742, Republic of Korea
[d]Department of Electrical and Computer Engineering, Ajou University, 206 Worldcup-ro, Suwon 16499, Republic of Korea

† Electronic supplementary information (ESI) available. See DOI: 10.1039/d1ta03678e

Open Access Article. Published on 21 June 2021. Downloaded on 2/16/2026 10:57:02 AM.
This article is licensed under a Creative Commons Attribution-NonCommercial 3.0 Unported Licence.

prominent parameters for optimizing their activity.[13,14] For example, by employing density functional theory (DFT) calculations, Shao *et al.* demonstrated that Pt NPs with a size of ~2.2 nm exhibited the maximum ORR mass activity and the weakest oxygen binding energy under $HClO_4$ conditions.[15] In addition, Sun *et al.* reported that Pt NPs with a size of 3–3.5 nm showed the highest HOR mass activity in H_2SO_4 and explained their findings in terms of the fraction of edge sites and facet fractions.[16] Furthermore, Ohyama *et al.* reported that Ru NPs with a size of ~3 nm exhibited the maximum activity, attributed to the optimal crystallinity and the roughened surface of the NPs.[17] These findings indicate that an optimal crystal structure and the fine control of Ru NP size are highly desired toward enhancing their HOR activity.

Atomic layer deposition (ALD) has been considered as a promising method for synthesizing metal NPs on a high surface area support. In principle, the ALD process is based on the sequential, self-limiting reaction of precursors and the interaction between the substrate and the precursor molecules.[18] Therefore, it is possible to efficiently control the size and obtain the uniformity of NPs owing to its ability to achieve atomic-scale and conformal coating on nonplanar and high aspect-ratio structures, as well as to offer the advantages such as its simplicity and non-additional processes compared to wet-based methods.[19,20] In most of the previous studies on the ALD technique, NPs are deposited on flat substrates or static stages such as on carbon aerogels, graphene (supported onto glass slides), graphene nanosheets, and carbon nanotubes (CNTs) transferred on a quartz wafer.[21–23] However, the non-uniform dispersion of the NPs throughout the film matrix affects their mass production as powder catalysts for fuel cells, thus hampering their commercialization. Therefore, it is important to improve the large-scale uniformity of NPs within the matrix of porous substrates. A fluidized bed reactor (FBR)-ALD system is a promising scalable synthesis technique for improving the uniformity of NPs in the matrix of the substrate owing to its efficient flow of precursor and gas inside the deep regions of the porous particles (substrates).[24] Recently, our group reported the synthesis of highly uniform Pt catalysts by FBR-ALD and observed that the Pt catalyst exhibited improved catalytic performance compared to commercial Pt catalyst with a similar Pt wt% due to higher uniformity.[15,25] Nevertheless, to the best of our knowledge, Ru NPs supported on carbon powder synthesized by ALD have been rarely reported. In addition, due to its excellent uniformity, ALD can shed light on the effects of the accurate NP size compared to the wet process.

Therefore, in this study, a Ru catalyst with highly dispersed and size-controllable NPs was synthesized by FBR-ALD by controlling the deposition parameters. The structural properties and electrochemical characteristics of the Ru catalysts under alkaline conditions were systematically investigated as a function of the Ru NP sizes. The effect of the NP size on the HOR activity of the Ru catalyst in an alkaline electrolyte was demonstrated. The 10 ALD cycled Ru catalyst with a NP size of ~2 nm exhibited the highest mass activity owing to its electrochemically favourable active roughened surface with desirable crystallinity. In addition, hydrogen binding energy (HBE) calculations revealed that the specific activity of the catalyst increased with decreasing HBE, and the HOR of the catalyst was enhanced under alkaline conditions owing to the weakening of the metal–H interaction.

2. Experimental

A. FBR-ALD process for synthesizing the Ru catalyst

Herein, Ru catalysts were deposited on acid-treated carbon black (Vinatech Co. Ltd., VFC-SP0450) (ESI and Fig. S1†) by using an FBR-ALD system (i-SAC research, iPV-d100). To properly fluidize the carbon black, size-selected carbon black was prepared in a range from 60–100 μm using two different sieve sizes. Before inserting the carbon black into the reactor, glass beads (1 mm, Glastechnique) were first added to fill the chamber to produce highly uniform gas transfers. The reactor containing the carbon black powder (0.4 g) was slowly evacuated using a rotary pump at 0.01 torr to avoid pumping out the powder. To this end, the FBR-ALD system was equipped with two pumping lines: a narrow pumping line for slow pumping and a wide line for the deposition process. The reactor and gas lines were heated at 300 °C and 100 °C, respectively. $Ru(CO)_3(\eta^4\text{-}C_6H_8)$ (i-Chem Co. Ltd.) was used as the Ru precursor (Fig. S2†) and was maintained at room temperature. Ultra-high purity (UHP, 99.999%) O_2 gas was used as the reactant. Before the first ALD cycle, a pre-process was carried out with Ar gas at 50 sccm (30 s), and then at 100 sccm (60 s) to prevent the abrupt fluidization of the powder. Subsequently, ALD cycles were carried out to deposit Ru NPs on the carbon black, where each ALD cycle consisted of a $Ru(CO)_3(\eta^4\text{-}C_6H_8)$ pulse (120 s), a purge (90 s), a 30 sccm O_2 pulse (90 s), and another purge (90 s). During this process, 100 sccm of UHP Ar gas was continuously supplied into the reactor to bubble the $Ru(CO)_3(\eta^4\text{-}C_6H_8)$ precursor, thus purging and fluidizing the powder. The working pressure during deposition was sustained at 0.4 and 0.6 torr during the O_2 pulse step. A more detailed and additional experimental ALD process is included in the ESI.†

B. Characterization of the Ru catalysts

Thermogravimetric analysis (TGA, PerkinElmer, STA 6000) and inductively coupled plasma-mass spectroscopy (ICP-MS, Elan DRC II, PerkinElmer Sciex) were used to identify the wt% of Ru on carbon black. The TGA was conducted at a heating rate of 20 °C min^{-1} at temperatures ranging from 30 to 900 °C. The crystallinity of the NPs was investigated by X-ray diffraction (XRD, Bruker, D8 ADVANC) using Cu-Kα radiation at a wavelength of 1.5418 Å. The surface area and porous structure of the catalysts were investigated by Brunauer–Emmett–Teller analysis (BET, Micromeritics, ASAP 2010 analyzer). The chemical bonding composition of the catalyst was determined using X-ray photoelectron spectroscopy (XPS, Thermo Electron Corporation, MICROLAB 350). The particle size, particle dispersion, and particle density of the catalysts from the high-angle annular dark field scanning transmission electron microscopy (HAADF-STEM) image were analysed by field emission transmission electron microscopy (FE-TEM, FEI, Talos F200X) at an operating

 This journal is © The Royal Society of Chemistry 2021

Open Access Article. Published on 21 June 2021. Downloaded on 2/16/2026 10:57:02 AM.
This article is licensed under a Creative Commons Attribution-NonCommercial 3.0 Unported Licence.

voltage of 200 kV. The lattice of Ru NPs was also investigated by Cs-TEM (JEOL Ltd., Cold FEG).

C. Electrochemical measurements of the Ru catalysts

For the electrochemical measurements, an electrochemically rotating disk electrode (Autolab, PGSTAT302N) test was carried out in a three-electrode system. The system consisted of a glassy carbon working electrode with a diameter of 5 mm, an Ag/AgCl reference electrode, and a Pt foil counter electrode. The potential of the system was determined using a reversible hydrogen electrode (RHE). The glassy carbon electrode was polished with 1 μm Al_2O_3 powder and washed with DI water before the experiment. To prepare the Ru catalyst ink, 5 mg of Ru catalyst was dispersed in a solution mixture containing isopropanol (5 mL), Nafion solution (0.2 mL of 5 wt% solution), and DI water (39.8 mL), after which the solution was ultrasonicated. Subsequently, 15 μL of the ink was drop-cast onto the glassy carbon working electrode (10 μg_{Ru} cm^{-2}) and dried in a thermal oven at 80 °C. Cyclic voltammograms (CVs) were analysed in a 0.1 M NaOH electrolyte with a potential range of 0.05–0.9 V at a sweep rate of 50 mV s^{-1} in an N_2 saturated electrolyte. The HOR was conducted in a 0.1 M NaOH electrolyte, which was first saturated with N_2 for 30 min, and then bubbled with H_2 for 30 min. Before the HOR, linear sweep was repeated for pre-treatment from −0.05 to 0.9 V at 1 mV s^{-1}. Cu_{upd} stripping voltammetry was carried out in a N_2 purged 0.1 M H_2SO_4 solution with 2 mM $CuSO_4$ from 0.3 to 0.9 V at 10 mV s^{-1} after Cu deposition at 0.3 V (*vs.* RHE) for 100 s. Before the voltammetry, the catalysts were pre-treated by cyclic voltammetry from 0.1 V to 1 V at 500 mV s^{-1} in a 0.1 M H_2SO_4 solution without $CuSO_4$. For Ru/C, additional cyclic voltammetry pre-treatment was carried out from 0 to 0.01 V at 0.1 mV s^{-1} until the voltammogram was stable. The voltammogram in 0.1 M H_2SO_4 solution without $CuSO_4$ from 0.3 to 0.9 V at 10 mV s^{-1} was recorded as the background for the corresponding Cu_{upd} stripping voltammogram.

3. Results & discussion

During the ALD process, when the $Ru(CO)_3(\eta^4\text{-}C_6H_8)$ precursor is exposed to the surface, it chemically adsorbs and saturates with the surface, forming no more than one monolayer of chemically adsorbed species. During the purge time, the excess physisorbed precursors and the volatile by-products are evacuated. When O_2 is injected, it reacts with the chemisorbed layer of the precursor of which the ligand was combusted. The volatile by-products and the excess reactants are purged into the pumps during the next purge step. To check this ALD reaction, before synthesizing Ru powder catalysts, Ru thin films were deposited on a SiO_2 wafer by ALD using $Ru(CO)_3(\eta^4\text{-}C_6H_8)$ as the precursor. The ALD was performed as a function of the precursor pulse times with a fixed purge time of 10 s, a O_2 pulse of 5 s, and more purge time of 10 s at a substrate temperature of 300 °C. With increasing Ru precursor pulse times from 0.5 to 1 s, the growth rate of Ru thin films on the SiO_2 wafer increased and then saturated above 1 s (Fig. 1(a)). The saturation of the growth rate indicates the occurrence of a self-limiting reaction

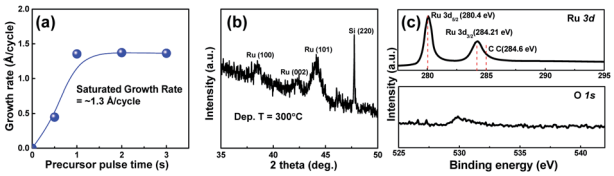

Fig. 1 (a) Growth rate of Ru thin films as a function of the precursor pulse times on a SiO_2 substrate (X s-precursor pulse, 10 s-purge, 5 s-O_2 reactant, and 10 s-another purge at 300 °C). (b) XRD spectra of the 30 nm-thick Ru thin films prepared on a SiO_2 wafer (1 s-precursor pulse, 10 s-purge, 5 s-O_2 reactant, and 10 s-another purge at 300 °C). (c) XPS analysis of Ru 3d and O 1s peaks for the deposited Ru thin films after Ar etching.

mechanism, which could be attributed to the nature of the ALD.[26] In addition, reflection peaks were observed along the (100), (200), and (101) planes in the XRD spectra of the Ru thin film, which corresponded to the formation of a crystalline hexagonal close-packed (HCP) Ru structure (Fig. 1(b)). Furthermore, no RuO_2 peaks were detected, which could be attributed to the formation of a high percentage of pure Ru metal in the films also identified by SIMS analysis (Fig. S3†). In addition, the XPS profiles of the Ru thin film revealed that the Ru film contained a negligible amount (~2%) of oxygen impurities (Fig. 1(c)), which consisted of Ru–O bonding and carbon bonding which could be attributed to the ligands of the precursor and chemisorbed surface oxygen (Fig. S4†).[27,28] These results indicate that pure Ru NPs can be grown on the surface of carbon black by ALD using $Ru(CO)_3(\eta^4\text{-}C_6H_8)$.

The Ru catalysts were synthesized by FBR-ALD as a function of the ALD cycles to control the size of the Ru catalyst as illustrated in Fig. 2(a). It was noted that the surface area of carbon black is much higher than that of the SiO_2 wafer. Therefore, the saturated Ru wt% depending on longer Ru precursor times (120 s) was confirmed, ensuring that the ALD Ru NPs on the carbon support were successfully formed with the optimized ALD cycles (Fig. S5†). The wt% of the Ru NPs on carbon was calculated by ICP and TGA (Fig. 2(b) and S6†). With an increase in the number of ALD cycles from 5 to 30 cycles, the Ru wt% increased from ~5 to ~32 wt%. To investigate the extent of the Ru loading on carbon, the Ru mass as a function of the ALD cycles was calculated (Fig. 2(c)).[29] As shown in the figure, the extrapolated line passed through the *x*-axis close to the origin, indicating the existence of a short nucleation delay normally identified in ALD-metal growth, which is considered to have no significant impact

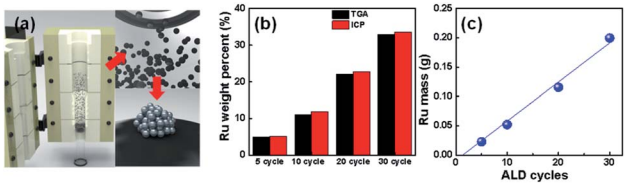

Fig. 2 (a) Schematics of the deposition process of the Ru catalyst by FBR-ALD. (b) Ru wt% as a function of the ALD cycles analysed by ICP and TGA. (c) Ru mass depending on the ALD cycles.

Open Access Article. Published on 21 June 2021. Downloaded on 2/16/2026 10:57:02 AM.
This article is licensed under a Creative Commons Attribution-NonCommercial 3.0 Unported Licence.

on the uniform Ru NP growth. In addition, with an increase in the number of ALD cycles, the Ru mass increased linearly, and a self-limiting phenomenon was also observed,[20] demonstrating a relatively constant growth rate of Ru on carbon. The more detailed and proposed ALD process included in the illustration using $Ru(CO)_3(\eta^4\text{-}C_6H_8)$ and O_2 is discussed in Fig. S7.†

To obtain the visible image of the Ru NPs on the carbon substrate, TEM analysis was conducted. Fig. 3(a) shows the low-magnification HAADF-STEM image of the 30 cycled ALD Ru catalyst. As shown in the image, the Ru NPs were uniformly synthesized on the carbon black over a wide range of areas despite high Ru loadings. The energy dispersive spectroscopy (EDS) images of C (Fig. 3(b)) and Ru (Fig. 3(c)) in the catalyst confirmed the excellent uniformity of the Ru catalyst on the carbon support. In contrast, as shown in Fig. 3(d), the commercial Ru catalyst exhibited partly non-uniform and agglomerated NPs, which can deteriorate the stability and efficient surface of the Ru catalyst. To elucidate the NP size and density, a high magnification STEM image was investigated as shown in Fig. 3(e)–(h), which is extracted from each low magnification image indicated by Fig. S8.† With an increase in the number of ALD cycles, the size of the Ru NPs increased from ~1.7 to 3.8 nm (Fig. S9†). Highly dense Ru NPs were observed after 5 cycles, and even after 30 cycles (Fig. 3(h)), the Ru NPs were dense and not randomly agglomerated, indicating a relatively uniform size distribution. Uniformly dispersed and dense Ru NPs were nucleated on a number of functional groups on the carbon during the initial cycles.[30] However, at higher cycles, the Ru NPs coalesced, resulting in an increased NP size. The 30 cycled Ru NPs exhibited a relatively uniform distribution without new nucleation on the carbon surface. In addition, the uniform, dense, and narrow size distribution of Ru NPs was confirmed compared to the commercial Ru catalyst with a wide range of size distributions, as shown in Fig. S10.†

To investigate the effect of the ALD cycle on the size of the Ru NPs, the crystal structure, textural characteristics, and binding energy of the Ru NPs were investigated. Fig. 4(a) shows the pore-size distribution curves exhibiting the mesopore and macropore distribution in the catalyst. After the deposition of the Ru NPs on the carbon support, the peak intensity of the mesopores in the carbon decreased continuously with increasing ALD cycles and decreasing BET surface area (Table S1†). This could be attributed to the filling of the mesopores by the Ru loadings.[31] Fig. 4(b) shows the XRD results of the Ru catalysts as a function of the ALD cycles. The peaks observed at 38.4°, 42.2°, and 44.0° corresponded to HCP Ru (100), (002), and (101), respectively. In addition, no crystal peaks were observed in the XRD pattern of the 5 cycled Ru catalyst, which could be due to an amorphous structure, relatively low content of Ru NPs compared to that of the carbon material or overlapping the very small intense peaks with carbon peak. However, with an increase in the number of ALD cycles, the Ru peak intensity emerged and became sharper, indicating an increase in the Ru NP size, as indicated by the decrease in the full width at half maximum. In addition, the (101) peak of Ru NPs became the preferred orientation upon increasing the cycles. H. Inoue *et al.* reported that the (101) peak of Ru NPs signifies a higher structural sensitivity and HOR activity than other planes, suggesting that H_2 may be easily absorbed on a coordinatively unsaturated atom in the ridges of the (101) surface;[32] therefore, it can be anticipated that Ru NPs with the preferred orientation along (101) by ALD can allow a better HOR reaction. The size of Ru NPs has a significant effect on their chemical status. To observe the binding state of the Ru catalysts with increasing the number of cycles, XPS analysis was performed, and the results are shown in Fig. 4(c) and (d). With increasing ALD cycles, the intensities of the Ru $3p_{3/2}$ and $3p_{1/2}$ peaks increased (Fig. 4(c)); however, there was no significant shift in the position of these peaks, indicating that the chemical environment of the Ru species in all the synthesized samples was similar, as shown in Fig. S11(a)–(d).† For the oxygen binding state (Fig. 4(d)), the XPS analysis revealed that the bare carbon consisted of oxidation binding energies such as C–O,

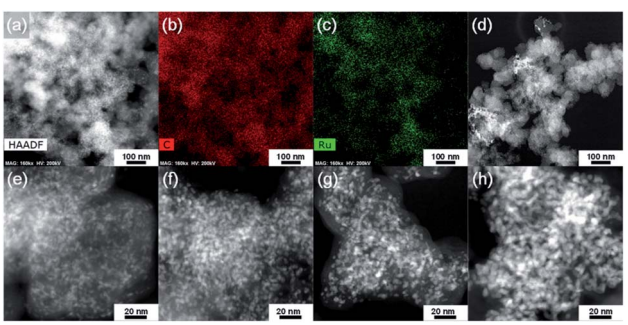

Fig. 3 (a) HAADF-STEM image of the Ru catalyst with 30 cycles (~32 wt%) synthesized by FBR-ALD. TEM-EDS images of (b) C element and (c) Ru element, corresponding to (a). (d) HAADF-STEM images of the commercial Ru catalyst (Premetek, 20 wt%) and the FBR-ALD-synthesized Ru catalysts as a function of the number of ALD cycles: (e) 5 cycles, (f) 10 cycles, (g) 20 cycles and (h) 30 cycles.

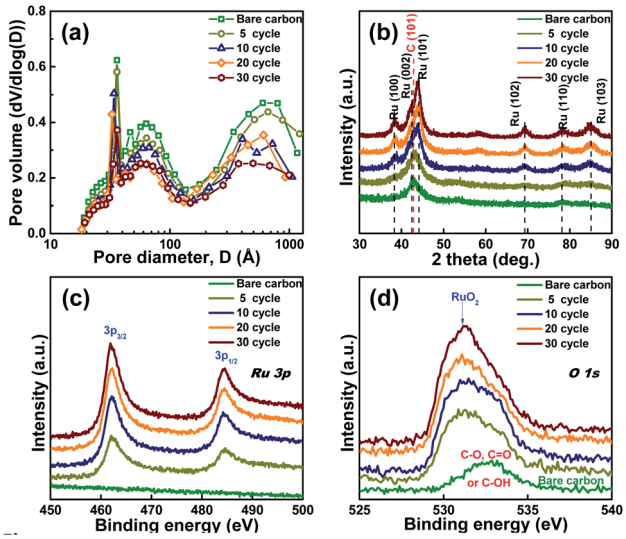

Fig. 4 (a) Pore size distribution of the Ru catalysts as a function of the ALD cycles. (b) XRD patterns and XPS profile of (c) Ru 3p and (d) O 1s of ALD-Ru catalysts.

This journal is © The Royal Society of Chemistry 2021

Open Access Article. Published on 21 June 2021. Downloaded on 2/16/2026 10:57:02 AM.
This article is licensed under a Creative Commons Attribution-NonCommercial 3.0 Unported Licence.

C=O, and C–OH. After the deposition of the Ru NPs on the carbon surface, Ru–O and Ru–OH were formed.

With an increase in the number of cycles, the peak intensity increased, which could be attributed to the increase in the Ru metal content on the carbon surface, as shown in Fig. S11(e)–(h).† However, the peak patterns were maintained with an increase in the Ru NP growth, with no significant change in the composition and binding state of Ru NPs with an increase in the size of the Ru NPs and even at low 5 cycles during the ALD process.

To demonstrate the appropriate crystallinity and structural characteristics of the Ru NPs, Cs-TEM and HR-TEM were carried out for the 10 cycled, 30 cycled, and commercial Ru catalysts (Fig. 5). The 5 cycled Ru NP sample exhibited an amorphous-like structure, which could be attributed to the existence of Ru oxide species within the Ru NPs (Fig. S12†). This amorphous structure can reduce the electrochemical activity of the catalyst due to its high susceptibility to the formation of surface oxygenated species, which can inhibit the absorption of H_2.[17] However, some disordered lattices and crystalline lattice fringes with various lattice planes of (101), (100), and (002) were observed in the 10 cycled Ru NPs with ~2 nm size as shown in Fig. 5(a). This result suggests that the Ru NPs were covered with amorphous-like layers, resulting in the formation of a roughened surface,[17] which exhibited an indistinct fast Fourier transform (FFT) pattern. In contrast, after 30 cycles, highly crystalline Ru NPs were observed (Fig. 5(b)), as confirmed from the FFT pattern and XRD data. For the commercial Ru NPs with an average size of 3.83 nm, a ~2 nm NPs was selectively found out (Fig. 5(c)) and then it was observed that Ru NPs consisted of partly amorphous and poor crystalline structures, as indicated in their FFT patterns and inverse lattice in the inset figure. It indicates that ALD can cause better crystallization of Ru NPs than the commercial catalyst which is confirmed by the comparison of XRD crystallinity between the ALD Ru catalyst and commercial Ru catalyst with a similar wt% (Fig. S13†).

These Ru NP characteristics such as dispersion, uniformity, size, and crystal structure can significantly influence the HOR. To evaluate the catalytic activity of the Ru catalysts synthesized by FBR-ALD, electrochemical analysis was performed, and the results were compared to those of commercial Ru catalysts. Fig. 6(a) shows the CVs of the Ru catalysts as a function of the ALD cycles in a 0.1 M NaOH aqueous solution. The anodic peak (0.05–0.3 V) originated from the desorption of underpotentially deposited hydrogen and Ru surface oxidation.[33] With an increase in the number of ALD cycles, the anodic peak shifted to a higher potential, which could be related to the HBE. In addition, with a decrease in the number of ALD cycles, the Ru surface oxidation peak increased. To examine the electrochemical surface area (ECSA) of the catalyst, Cu_{upd} stripping voltammetry was performed in a N_2-purged 0.1 M H_2SO_4 solution containing 2 mM $CuSO_4$ (Fig. 6(b)). As shown in Table S2,†

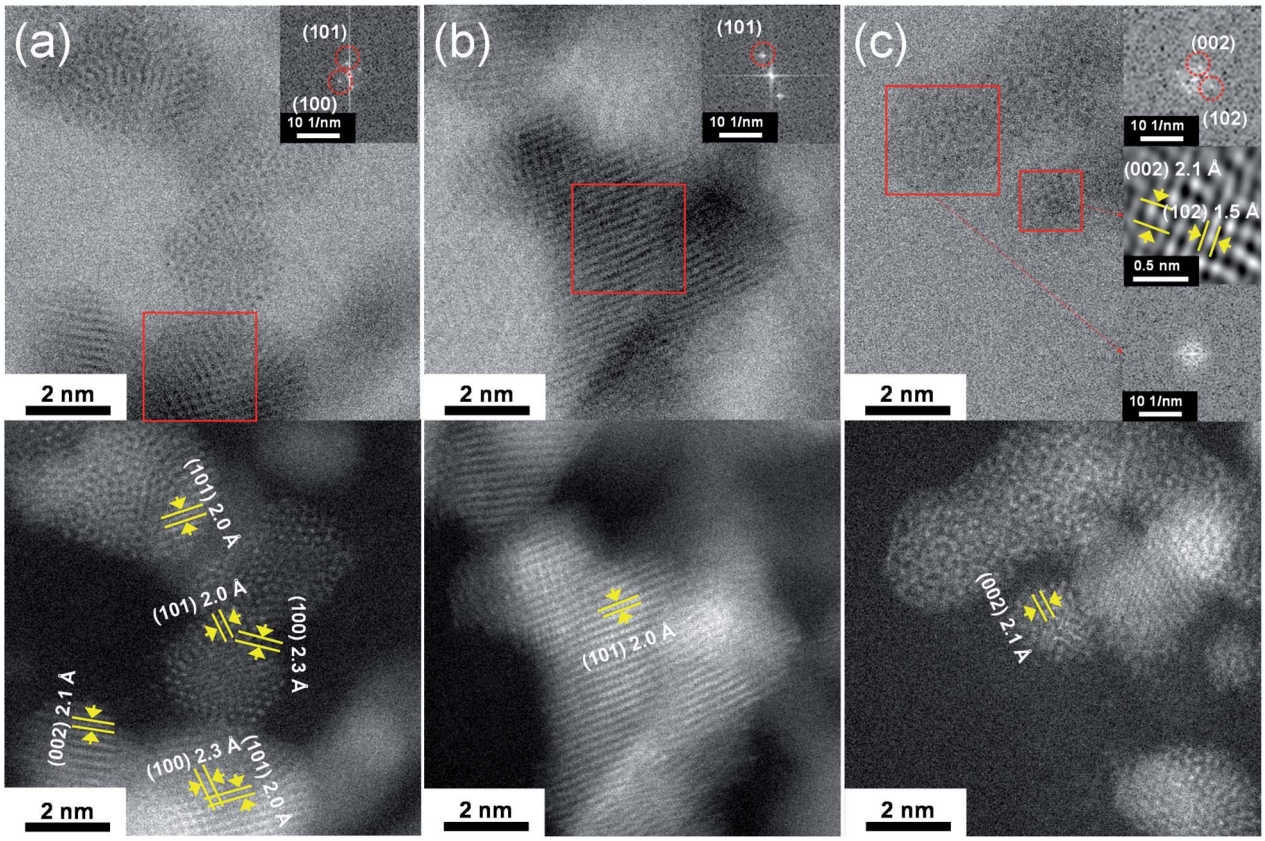

Fig. 5 HR-TEM and Cs-TEM images of (a) 10 cycled and (b) 30 cycled Ru catalysts synthesized by FBR-ALD, and (c) the commercial Ru catalyst (20 wt%, Premetek).

Open Access Article. Published on 21 June 2021. Downloaded on 2/16/2026 10:57:02 AM.
This article is licensed under a Creative Commons Attribution-NonCommercial 3.0 Unported Licence.

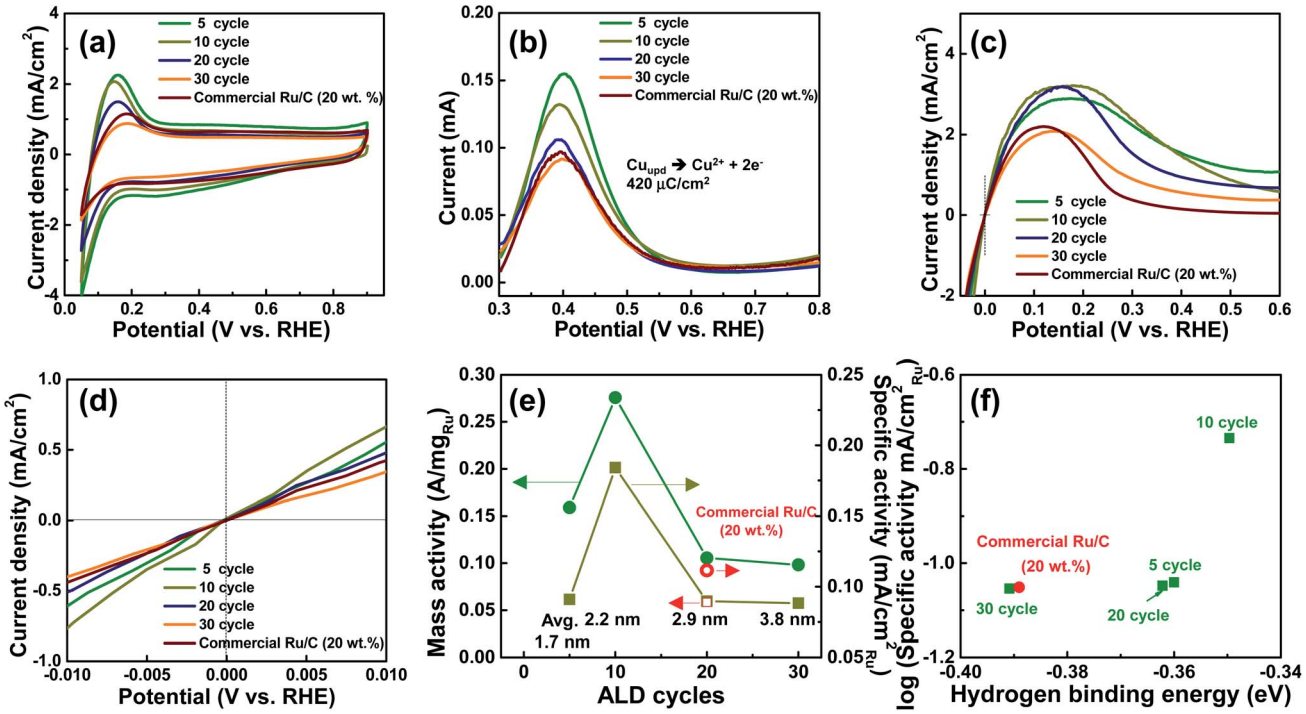

Fig. 6 (a) Cyclic voltammetry, (b) Cu_{upd} stripping voltammograms, (c) polarization curve, (d) low overpotential region of the polarization curve, and (e) mass and specific activities of the Ru catalysts as a function of the ALD cycles (*iR*-corrected). (f) Hydrogen binding energy *vs.* specific activity of the respective samples. The commercial Ru catalyst (Premetek, 20 wt%) used as a reference was included in all graphs.

the ECSA results revealed that the 5 cycled Ru catalyst exhibited the highest Ru active area owing to the efficient Ru surface resulting from the small NP size. In addition, compared to the commercial Ru catalysts, the 20 cycled Ru catalyst with a similar wt% exhibited a higher ECSA, which could be attributed to its uniformity and high NP density as explained in Fig. 3. Fig. 6(c) shows the linear sweep voltammogram (LSV) of the catalyst in 0.1 M NaOH aqueous solution saturated with H_2 at 2500 rpm. The exchange current density (i_0) was obtained from the Butler–Volmer equation in a low overpotential region (η) from −0.01 to 0.01 V, as shown in Fig. 6(d).

$$i = i_0(2F/RT) \times \eta \quad (1)$$

where i_0 is the measured current density, F is Faraday's constant, R is the gas constant, and T is the absolute temperature. The i_0 value was calculated from the slope of the low overpotential region polarization curve and the value of each catalyst was normalized using the weight of Ru on the disk electrode and ECSA to determine the mass activity (MA) and specific activity (SA), respectively (Fig. 6(e)). With an increase in the number of ALD cycles from 5 to 10 cycles, the MA values of the catalyst increased. In addition, although the 5 cycled Ru catalyst exhibited the highest ECSA value, its MA value was lower than that of the 10 cycled Ru catalyst due to the relatively higher charge transfer resistance within the thick catalyst layer, as demonstrated from the electrochemical impedance spectroscopy (EIS) results in Fig. S14.† With an increase in the wt% of Ru and ALD cycles, the 10 cycled Ru catalyst exhibited the highest MA and SA; however, the activities decreased with a further increase in the wt% of Ru and ALD cycles, which could be attributed to the lower ECSA due to the larger average NP size. The optimal NP size with the most active surface area for achieving enhanced activities was 2.2 nm. Finally, the HBE (E_{M-H}) of the catalyst was calculated using the H_{UPD} desorption peak on the CV according to the following equation:[10,34]

$$E_{M-H} = -E_{peak}F - 1/2TS \quad (2)$$

where F is Faraday's constant, T is the temperature (298 K), and S is the entropy of H_2 under standard conditions. Fig. 6(f) shows the SA as a function of the HBEs. The SA of the catalyst increased with a decrease in the HBE. Upon increasing cycles from 5 to 30 cycles, HBE showed a non-linear plot, indicating that the HBE of Ru catalysts obtained by ALD was affected by the change in the surface structure and characteristics probably resulting from the fraction of the coordinatively unsaturated or saturated Ru atoms as well as their size. Previous studies have reported that a decrease of HBE enhances the HOR of catalysts under alkaline conditions owing to the weakening of the metal–H interaction,[9] resulting in the best performance of the 10 cycled Ru catalyst obtained by ALD.

The size-dependent and non-linear HOR activity of the catalyst can be also explained based on their structural characteristics. Previous studies have reported that the roughened surface of Ru metal is a reactive structure for an efficient HOR in an alkaline atmosphere and that the ~3 nm-sized Ru catalyst synthesized by the wet process was an optimal NP catalyst for

 This journal is © The Royal Society of Chemistry 2021

Open Access Article. Published on 21 June 2021. Downloaded on 2/16/2026 10:57:02 AM.
This article is licensed under a Creative Commons Attribution-NonCommercial 3.0 Unported Licence.

achieving the highest MA, as well as excellent cell performance.[17] However, in this present study, the optimal size is shifted to ~2 nm and this size exhibited the highest HOR, MA, and SA owing to its roughened surface with desirable crystallinity, which can be much more reliable for optimization due to the excellent uniform NP dispersion. The results achieved in this work are significantly higher than those of the Pt catalyst (Premetek, 20 wt%, Fig. S15†), previously reported Ru catalysts as well as other metal catalysts (Table S3†). According to previous reports,[35–37] the synthesis of metal NPs with size less than ~3 nm by the wet chemical processes may mostly construct an amorphous structure which is not enough crystalline to get better electrochemical activity. On the other hand, it was reported that ALD can provide relatively pure noble metal deposition[38,39] based on the chemisorption of the precursor indicated in this study (Fig. 1(c)) as well, resulting in a highly crystalline structure of Ru NPs. The small size of the Ru NPs with roughened surfaces (combination amorphous and crystalline) synthesized in this study are advantageous for enhancing the HOR of the catalyst owing to their high surface area and desirable crystallinity. To the best of our knowledge, there are no studies on the synthesis of highly active Ru NPs with a size of ~2 nm (without any organic ligands) by the wet chemical methods, which could be attributed to the overgrowth of the amorphous moiety at the initial stage. However, this initial amorphous growth was controlled at the atomic scale by the FBR-ALD technique, which enabled the synthesis of very small (~2 nm) and electrochemically active Ru NPs. In addition, the MA and SA of the 20 cycled Ru catalysts (~20 wt%) were higher than those of commercial Ru/C with a similar wt%, which could be attributed to the high uniformity and dispersion of the Ru NPs synthesized by the FBR-ALD process as well as than those of the Pt catalyst (Fig. S15 and Table S4†). Thus, FBR-ALD can be regarded as a more favourable technique for synthesizing small but active catalysts for the HOR.

4. Conclusions

In summary, carbon-supported Ru NPs with controllable size and crystallinity were synthesized by a FBR-ALD process, considering pure Ru deposition at the thin film stage on a SiO_2 substrate using $Ru(CO)_3(\eta^4\text{-}C_6H_8)$ and O_2 reactants. Subsequently, Ru NPs were deposited on a carbon support as a function of the number of ALD cycles from 5 to 30 cycles. TGA and ICP revealed the self-limiting mechanism of the Ru catalyst. Controlling the ALD cycles, uniform and dense Ru NPs with tuneable sizes were successfully synthesized. Even at a smaller Ru NP size (~2.2 nm), a thin amorphous layer covered the crystalline structure, which was found to be highly advantageous to improve the HOR whereas commerical Ru NPs exhibited a significantly lower crystallinity at a similar size. ECSA calculations revealed that the 5 cycled Ru catalyst exhibited the highest ECSA owing to its efficient Ru surface area due to its smaller size. However, the 10 cycled Ru catalyst with an NP size of ~2.2 nm exhibited higher HOR activity than the 5 cycled Ru catalyst owing to its higher charge transfer resistance resulting from the higher carbon content. The ALD-synthesized Ru catalyst also outperformed the commercial Ru/C catalyst with a similar wt%. HBE calculations revealed that the HOR of the catalyst was enhanced under alkaline conditions owing to the weakening of the metal–H interaction. The findings of this study will provide useful insight for the synthesis of efficient and scalable Ru or Ru-based bimetallic catalysts with optimal size and crystallinity (roughness) by FBR-ALD to enhance the performance of anode electrodes in fuel cells.

Conflicts of interest

There are no conflicts to declare.

Acknowledgements

This research was supported by the Basic Science Research Program through the National Research Foundation of Korea (NRF) funded by the Ministry of Education (2020R1A6A3A01097578) and funded by the Korea government (MSIT) (No. 2020R1A2C101484112).

Notes and references

1 A. Faur Ghenciu, *Curr. Opin. Solid State Mater. Sci.*, 2002, **6**, 389–399.
2 H. Adabi Firouzjaie and W. E. Mustain, *ACS Catal.*, 2020, **10**, 225–234.
3 K. F. L. Hagesteijn, S. Jiang and B. P. Ladewig, *J. Mater. Sci.*, 2018, **53**, 11131–11150.
4 D. S. Kim, A. Labouriau, M. D. Guiver and Y. S. Kim, *Chem. Mater.*, 2011, **23**, 3795–3797.
5 D. R. Dekel, *J. Power Sources*, 2018, **375**, 158–169.
6 J. R. Varcoe, P. Atanassov, D. R. Dekel, A. M. Herring, P. A. Kohl, A. R. Kucernak, W. E. Mustain, K. Nijmeijer, K. Scott, T. Xu and L. Zhuang, *Energy Environ. Sci.*, 2014, **7**, 3135–3191.
7 W. Sheng, H. A. Gasteiger and Y. Shao-Horn, *J. Electrochem. Soc.*, 2010, **157**, B1529–B1536.
8 J. Durst, A. Siebel, C. Simon, F. Hasche, J. Herranz and H. A. Gasteiger, *Energy Environ. Sci.*, 2014, **7**, 2255–2260.
9 Y. Wang, G. Wang, G. Li, B. Huang, J. Pan, Q. Liu, J. Han, L. Xiao, J. Lu and L. Zhuang, *Energy Environ. Sci.*, 2015, **8**, 177–181.
10 J. Ohyama, D. Kumadaa and A. Satsuma, *J. Mater. Chem. A*, 2016, **4**, 15980–15985.
11 J. Ohyama, T. Sato and A. Satsuma, *J. Power Sources*, 2013, **225**, 311–315.
12 L. Ma, A. Hsu and R. Chen, *J. Power Sources*, 2013, **241**, 696–702.
13 J. Zheng, S. Zhou, S. Gu, B. Xu and Y. Yan, *J. Electrochem. Soc.*, 2016, **163**, F499–F506.
14 W.-J. Lee, S. Bera, H.-C. Shin, W.-P. Hong, S.-J. Oh, Z. Wan and S.-H. Kwon, *Adv. Mater. Interfaces*, 2019, **6**, 1901210.
15 M. Shao, A. Peles and K. Shoemaker, *Nano Lett.*, 2011, **11**, 3714–3719.
16 Y. Sun, Y. Dai, Y. Liu and S. Chen, *Phys. Chem. Chem. Phys.*, 2012, **14**, 2278–2285.

Open Access Article. Published on 21 June 2021. Downloaded on 2/16/2026 10:57:02 AM.
This article is licensed under a Creative Commons Attribution-NonCommercial 3.0 Unported Licence.

17 J. Ohyama, T. Sato, Y. Yamamoto, S. Arai and A. Satsuma Size, *J. Am. Chem. Soc.*, 2013, **135**, 8016–8021.
18 C.-T. Hsieh, W.-Y. Chen, D.-Y. Tzou, A. K. Roy and H.-T. Hsiao, *Int. J. Hydrogen Energy*, 2012, **37**(23), 17837–17843.
19 S.-H. Kwon, O.-K. Kwon, J.-H. Kim, H.-R. Oh, K.-H. Kim and S.-W. Kang, *J. Electrochem. Soc.*, 2008, **155**, H296–H300.
20 H.-B.-R. Lee, K. L. Pickrahn and S. F. Bent, *J. Phys. Chem. C*, 2014, **118**, 2325–12332.
21 C.-T. Hsieh, W.-Y. Chen, D.-Y. Tzou, A. K. Roy and H.-T. Hsiao, *Int. J. Hydrogen Energy*, 2012, **37**(23), 17837–17843.
22 J. S. King, A. Wittstock, J. Biener, S. O. Kucheyev, Y. M. Wang, T. F. Baumann, S. K. Giri, A. V. Hamza, M. Baeumer and S. F. Bent, *Nano Lett.*, 2008, **8**(8), 2405–2409.
23 C. Liu, C.-C. Wang, C.-C. Kei, Y.-C. Hsueh and T.-P. Perng, *Small*, 2009, **13**, 1535–1538.
24 B. J. O'Neill, D. H. K. Jackson, J. Lee, J. Canlas, P. C. Stair, C. L. Marshall, J. W. Elam, T. F. Kuech, J. A. Dumesic and G. W. Hube, *ACS Catal.*, 2015, **5**, 1804–1825.
25 W.-J. Lee, S. Bera, C. M. Kim, E.-K. Koh, W.-P. Hong, S.-J. Oh, Z. Wan, E. Cho and S.-H. Kwon, *NPG Asia Mater.*, 2020, **12**, 40.
26 T. Aaltonen, M. Ritala, T. Sajavaara, J. Keinonen and M. Leskela, Atomic Layer Deposition of Platinum Thin Films, *Chem. Mater.*, 2003, **15**, 1924–1928.
27 J. Xu, J. Li, Z. Lian, A. Araujo, Y. Li, B. Wei, Z. Yu, O. Bondarchuk, I. Amorim, V. Tileli and B. Li, *ACS Catal.*, 2021, **11–6**, 3402–3413.
28 J. Xu, T. Liu, J. Li, B. Li, Y. Liu, B. Zhang, D. Xiong, I. Amorim, W. Li and L. Liu, *Energy Environ. Sci.*, 2018, **11**, 1819–1827.
29 C. Lin, J. B. Jang, L. Zhang, E. A. Stach and R. J. Gorte, *ACS Catal.*, 2018, **8**, 7679–7687.
30 W. Setthapun, W. D. Williams, S. M. Kim, H. Feng, J. W. Elam, F. A. Rabuffetti, K. R. Poeppelmeier, P. C. Stair, E. A. Stach, F. H. Ribeiro, J. T. Miller and C. L. Marshall, *J. Phys. Chem. C*, 2010, **114**, 9758–9771.
31 W. Shen, X. Yang, Q. Guo, Y. Liu, Y. Song, Z. Han, Q. Sun and J. Cheng, *Mater. Lett.*, 2006, **60**, 3517–3521.
32 H. Inoue, J. X. Wang, K. Sasaki and R. R. Adzic, *J. Electroanal. Chem.*, 2003, **554–555**, 77–85.
33 H. A. Gasteiger, N. M. Markovic and P. N. Ross, *J. Phys. Chem.*, 1995, **99**, 3411–3415.
34 W. Sheng, Z. Zhuang, M. Gao, J. Zheng, J. G. Chen and Y. Yan, *Nat. Commun.*, 2015, **6**, 5848.
35 K. Murata, Y. Mahara, J. Ohyama, Y. Yamamoto, S. Arai and A. Satsuma, *Angew. Chem.*, 2017, **129**, 16209–16213.
36 Z. Zhang, J. Song, Z. Jiang, Q. Meng, P. Zhang and B. Han, *ChemCatChem*, 2017, **9**, 2448–2452.
37 A. Roy, M. R. Talarposhti, S. J. Normile, I. V. Zenyuk, V. D. Andrade, K. Artyushkova, A. Serov and P. Atanassov, *Sustainable Energy Fuels*, 2018, **2**, 2268–2275.
38 W. J. Lee, Z. Wan, C.-M. Kim, I.-K. Oh, R. Harada, K. Suzuki, E.-A. Choi and S.-H. Kwon, *Chem. Mater.*, 2019, **31**, 5056–5064.
39 J. Gatineau, K. Yanagita and C. Dussarrat, *Microelectron. Eng.*, 2006, **83**, 2248–2252.

This journal is © The Royal Society of Chemistry 2021